

¹ To the Graduate Council:
² I am submitting herewith a thesis written by Jason Bane entitled “The EMC Effect
³ in A=3 Nuclei.” I have examined the final paper copy of this thesis for form and
⁴ content and recommend that it be accepted in partial fulfillment of the requirements
⁵ for the degree of Doctor of Philosophy, with a major in Nuclear Physics.

⁶
⁷

Nadia Fomin, Major Professor

⁸ We have read this thesis
⁹ and recommend its acceptance:

¹⁰ _____

¹¹ Jamie Coble

¹² _____

¹³ Kate Jones

¹⁴ _____

¹⁵ Thomas Papenbrock

¹⁶ _____

¹⁷ Soren Soreson

¹⁸

Accepted for the Council:

¹⁹
²⁰

Carolyn R. Hodges

²¹

Vice Provost and Dean of the Graduate School

²² To the Graduate Council:
²³ I am submitting herewith a thesis written by Jason Bane entitled “The EMC Effect
²⁴ in A=3 Nuclei.” I have examined the final electronic copy of this thesis for form and
²⁵ content and recommend that it be accepted in partial fulfillment of the requirements
²⁶ for the degree of Doctor of Philosophy, with a major in Nuclear Physics.

²⁷ Nadia Fomin, Major Professor

²⁸ We have read this thesis
²⁹ and recommend its acceptance:

³⁰ Jamie Coble

³¹ _____
³²

³³ Kate Jones

³⁴ _____
³⁵

³⁶ Thomas Papenbrock

³⁷ _____
³⁸

³⁹ Soren Soreson

⁴⁰ _____
⁴¹

⁴² Accepted for the Council:

⁴³
⁴⁴ Carolyn R. Hodges

⁴⁵ _____
⁴⁶

⁴⁷ Vice Provost and Dean of the Graduate School

⁴⁸ (Original signatures are on file with official student records.)

49

The EMC Effect in A=3 Nuclei

50

A Thesis Presented for

51

The Doctor of Philosophy

52

Degree

53

The University of Tennessee, Knoxville

54

Jason Bane

55

December 2018

⁵⁶

© by Jason Bane, 2018

⁵⁷

All Rights Reserved.

⁵⁸ Contents

⁵⁹	List of Tables	v
⁶⁰	List of Figures	vi
⁶¹	1 Introduction	1
⁶²	1.1 Electron scattering	2
⁶³	1.1.1 Deep inelastic scattering	5
⁶⁴	1.2 EMC Effect	6
⁶⁵	1.3 MARATHON	9
⁶⁶	2 Experimental Setup	10
⁶⁷	2.1 Thomas Jefferson Lab	10
⁶⁸	2.1.1 CEBAF	10
⁶⁹	2.1.2 Hall A	12
⁷⁰	2.2 Target	17
⁷¹	2.3 High Resolution Spectrometers	19
⁷²	2.3.1 Vertical Drift Chambers	20
⁷³	2.3.2 Scintillators	22
⁷⁴	2.3.3 Cherenkov	22
⁷⁵	2.3.4 Shower Calorimeter	22
⁷⁶	2.3.5 Pion Rejector	22
⁷⁷	2.3.6 FPP Chambers	22

78	2.4 Trigger Setup	22
79	2.5 DAQ - Data Acquisition System	22
80	2.6 Kinematic Settings	22
81	3 Calibration	23
82	3.1 Beam Line	23
83	4 Data Analysis	26
84	5 Results	27
85	6 Simulation	28
86	6.1 Investigation	28
87	6.2 Transformation	29
88	6.3 Results	31
89	7 Conclusion	34
90	Bibliography	35

₉₁ **List of Tables**

₉₂ List of Figures

₉₃	1.1	Simple Feynman diagram of an electron scattering from a proton [7].	3
₉₄	1.2	Graph of the ratio of A/D structure functions vs x for Carbon [10].	7
₉₅	1.3	EMC effect from EMC, SLAC, and BCDMS [17]	8
₉₆	1.4	Graph of the ratio of A/D structure functions vs x for Carbon [10].	9
₉₇	2.1	Schematic Layout of CEBAF.	11
₉₈	2.2	A 3D drawing of Hall A.	12
₉₉	2.3	A schematic layout of the beam line in Hall. [1]	13
₁₀₀	2.4	BPM design diagram, from JLab instrumentation group. Beam direction is from left to right [23].	14
₁₀₂	2.5	BPM design diagram, looking down the beam line[23].	14
₁₀₃	2.6	Hall A Current Monitor components [4].	16
₁₀₄	2.7	Target Images	18
₁₀₅	2.8	A side view of a HRS [1].	20
₁₀₆	2.9	A view of both the left(top) and right(bottom) detector stacks inside the left and right HRS [1].	21
₁₀₈	2.10	A sketch of the two VDC planes in the HRSs with a particle traveling through the detector at 45° .[6].	22
₁₁₀	3.1	A schematic layout of a harp fork [23]	24
₁₁₁	3.2	The X and Y position for a Bulls eye scan for BPM calibration.	25

112	6.1 Example of the electron beam(red) with a energy of 2.5 GeV and the	
113	proton(blue) with angle of 45° in respect to the electron and with a	
114	momentum of 0.5 GeV/c.	29
115	6.2 Vector representations of the momentum for the incoming electron(red)	
116	and target proton(blue) with units of GeV for each phase of their	
117	transformations before scattering.	30
118	6.3 Vector representations of the momentum for the incoming electron(red)	
119	and target proton(blue) with units of GeV for each phase of their	
120	transformations after scattering).	32
121	6.4 Simulation results for fixed momentum protons. Three runs with	
122	unique proton momentum.	33

¹²³ **Chapter 1**

¹²⁴ **Introduction**

¹²⁵ Understanding the world around us is the goal of every scientist, from the chemist
¹²⁶ that experiments with the formation of atoms to the geologist exploring the process of
¹²⁷ rock formations. Nuclear physicists focus on studying the fundamental constituents
¹²⁸ of matter, the building blocks of nature. Physicist use scattering experiments at
¹²⁹ accelerator facilities, like CERN in Switzerland, DESY in Germany, BATES in
¹³⁰ Massachusetts, JLAB in Virginia, and many others, to study the protons and neutrons
¹³¹ and their constituents that make up a nucleus. These experiments allow physicists
¹³² to observe the internal structure of the nucleus and to investigate the interactions
¹³³ between the quarks and gluons. Many of the experiments are design to confirm a
¹³⁴ existing results while also expanding on unique ideas.

¹³⁵ In the last century, there have been numerous breakthroughs in the fields of nuclear
¹³⁶ and particle physics. Rutherford discovered the proton by bombarding light nuclei
¹³⁷ with alpha particles to produce



¹³⁸ This reaction allowed Rutherford to conclude that the Hydrogen nucleus was a
¹³⁹ constituent of an atomic nuclei [18]. In the late 1950s, experimental results published

140 by W. McAllister and R. Hofstadter exposed some of the eternal structure of the
141 proton [7, 15]. The European Muon Collaboration(EMC) produced results in the
142 early 1980s showing a differences between the internal structure of the deuterium
143 nucleus and Iron [20, 10]. The data received from scattering experiments using alpha
144 particles contain information about the target, the beam, and the interaction between
145 the two. Deciphering and analyzing this data can be convoluted because the cross-
146 section contains information about the internal structure of the target and the beam
147 along with the interaction and forces between the two [18].

148 1.1 Electron scattering

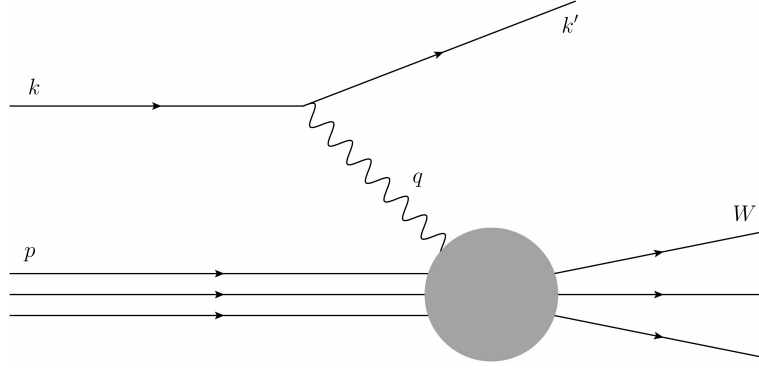
149 In order to remove some of the complexity in scattering experiments, one may
150 employ highly relativistic electrons. Electrons being point-like particles without any
151 internal structure allow the elimination of some of the analysis difficulties with using
152 alpha particles in scattering experiments due to their complex internal structure.
153 Electrons and the target nucleus, nucleon, or quarks interact via the exchange of
154 a virtual photon. Using quantum electrodynamics (QED), these interactions can
155 accurately be described by the well known electromagnetic interaction. Higher order
156 terms of this process contribute very little due to the coupling constant $\alpha \approx 1/137$,
157 being much smaller than one.

158 Figure 1.1 represents an electron scattering from a proton. The incoming or incident
159 electron's four-momentum is described as $k = (E, \vec{k})$ and the scattering electron's four-
160 momentum is represented by $k' = (E', \vec{k}')$. The exchange of the virtual photon in this
161 electromagnetic interaction is defined by the four-momentum transfer q :

$$Q^2 \equiv -q^2 = 4EE' \sin^2(\theta/2). \quad (1.2)$$

₁₆₂ In equation 1.2, E and E' are the electron energy before and after the scattering
₁₆₃ interaction. Theta is the angle that describes the deflection of E' from the electron's
₁₆₄ original path.

Figure 1.1: Simple Feynman diagram of an electron scattering from a proton [7].



₁₆₅ Along with Q^2 , the variables ν , W , and x_B are used to narrate the evolution of the
₁₆₆ electron scattering process. ν , defined as $p \cdot q/M$. In the rest frame of the target, ν
₁₆₇ can be described by:

$$\nu = E - E'. \quad (1.3)$$

₁₆₈ Simply, ν is the magnitude of energy loss by the electron during the scattering
₁₆₉ interaction. The invariant mass of the system, W , defines the hadronic state produced
₁₇₀ by the scattering event.

$$W^2 \equiv (q + p)^2 = M^2 + 2M\nu - Q^2. \quad (1.4)$$

₁₇₁ A scattering event with the invariant mass equal to the square of the mass of the
₁₇₂ nucleon, (M^2), falls in the regime of elastic scattering. W above M^2 will transform
₁₇₃ the scattering interaction from an elastic scattering to inelastic scattering due to
₁₇₄ the excited state of the scattered byproduct. x_B , the Bjorken scaling variable is a
₁₇₅ dimensionless quantity that measures the inelasticity of a scattering process. x_B is
₁₇₆ defined as: $x := \frac{Q^2}{2M\nu}$.

177 The intrinsic likelihood of an event with a certain Q^2 , ν , and W is defined by the
 178 scattering cross section. An electron scattering off of a target with a charge of $Z * e$
 179 can be described by the Rutherford cross-section. Povh et. al. details the Rutherford
 180 cross section as:

$$\left(\frac{d\sigma}{d\Omega} \right)_{Rutherford} = \frac{(zZe^2)^2}{(4\pi\epsilon_0)^2 * (eE_{kin})^2 \sin^4(\theta/2)}. \quad (1.5)$$

181 In the early 1920s, German physicists Stern and Gerlach performed an experiment
 182 that confirmed the presence of electron angular momentum. Later a discovery of
 183 electron spin was made by Uhlenbeck and Goudsmit. The Rutherford cross-section
 184 neglects the spin of an electron and its target. The Mott cross-section is the evolved
 185 version of the Rutherford cross-section. It has been modified to include the intrinsic
 186 spin of the target and electron. The Mott cross-section is: [12, 18]

$$\left(\frac{d\sigma}{d\Omega} \right)_{Mott} = \frac{4Z^2\alpha^2(\hbar c)^2 E'^2}{|\mathbf{q}_c|^4} \cos^2(\theta/2). \quad (1.6)$$

187 There is an agreement between the measured cross section and the theoretical Mott
 188 cross-section when in the limit of $|\mathbf{q}| \rightarrow 0$ for scattering events of electrons off of a
 189 target nuclei. As $|\mathbf{q}|$ climbs further from zero, the experimentally measured cross
 190 sections systematically decreases [18]. Increasing the $|\mathbf{q}|$ of an interaction reduces
 191 the size of the wavelength of the virtual photon that mediates the electromagnetic
 192 interaction between the electron and target nuclei and increases the resolution of the
 193 probe. The wavelength of this virtual photon is inversely proportional to $|\mathbf{q}|$, and can
 194 be described by the following: $\lambda = \frac{\hbar}{|\mathbf{q}|}$ [18]. Increasing the amount of momentum
 195 transferred in an electromagnetic reaction allows one to study deeper into the nucleus.

196 Studying the internal structure of a nucleus with the electromagnetic interaction
 197 requires increasing the momentum transferred. Pushing $|\mathbf{q}|$ to be comparable with the
 198 mass of a nucleon adds more complexity to the details of the scattering interaction.

199 At the appropriate levels of $|\mathbf{q}|$ to study the nucleons in the nucleus, the Mott cross-
 200 section equation requires modifications to include additional factors that incorporate
 201 information about the target. The Rosenbluth formula is based on the Mott
 202 cross section and embraces target recoil, magnetic moment, and charge and current
 203 distributions. Povh writes the Rosenbluth formula as:

$$\left(\frac{d\sigma}{d\Omega}\right) = \left(\frac{d\sigma}{d\Omega}\right)_{Mott} * \left[\frac{G_E^2(Q^2) + \tau G_M^2(Q^2)}{1 + \tau} + 2\tau G_M^2(Q^2) \tan^2 \frac{\theta}{2} \right]. \quad (1.7)$$

204 Equation 1.7 contains $G_E^2(Q^2)$ and $G_M^2(Q^2)$, the electric and magnetic form factors. τ
 205 is used in the Rosenbluth formalism to account for the magnetic moment of a nucleon
 206 and is defined as: $\tau = \frac{Q^2}{4M^2c^2}$ [18]. In the general case of electron scattering off of a free
 207 proton or neutron elastically, the scattered energy of the electron will be a function
 208 of the incident electron's energy and the scattered angle of the electron, shown in the
 209 following equation.

$$E' = \frac{E}{1 + \frac{E}{Mc^2}(1 - \cos\theta)} \quad (1.8)$$

210 1.1.1 Deep inelastic scattering

211 The first generation of electron scattering experiments achieving a significantly
 212 large $|\mathbf{q}|$ used a linear accelerator with a 25 GeV maximum beam energy, and
 213 following generations increased the total interaction energy to substantially higher
 214 thresholds. At these high incident beam energies, individual resonances cannot be
 215 separated in the invariant mass spectrum above 2.5 GeV. Observations made into
 216 this convoluted invariant mass spectrum has shown that many strongly interacting
 217 particles are produced, known as hadrons. Scattering interactions that generate
 218 these hadrons are considered to be inelastic. Inelastic scattering events contain
 219 the possibility of conceiving additional resultants and increase the complexity of
 220 a scattering interaction. Inelastic scattering events occur when the wavelength
 221 of the virtual photon is comparable to the radius of the struck nucleon or when
 222 $Q^2 R^2 \lesssim 1$ [18]. Increasing the amount of transferred momentum so that $Q^2 R^2 \gtrsim 1$,

increase the resolution of the probe to a level that allows for the interacting with
 the charge constituents within the nucleon. When the scattering event probes the
 fundamental elements of a nucleon, the scattering process is titled deep inelastic
 scattering(DIS). Due to the increase in complexity, an additional degree of freedom
 has to be introduced into the scattering cross section equation. Modifying the
 Rosenbluth formula to include the inelastic scattering structure functions $F_1(Q^2, \nu)$
 and $F_2(Q^2, \nu)$ evolves the Rosenbluth formula to contain the needed complexity of an
 inelastic event. These modifications are shown in equation 1.9.

$$\frac{d^2\sigma}{d\Omega dE'} = \left(\frac{d\sigma}{d\Omega} \right)_{Mott} \left[\frac{F_2(Q^2, \nu)}{\nu} + \frac{2F_1(Q^2, \nu)}{M} \tan^2 \frac{\theta}{2} \right] \quad (1.9)$$

[21] [13]

1.2 EMC Effect

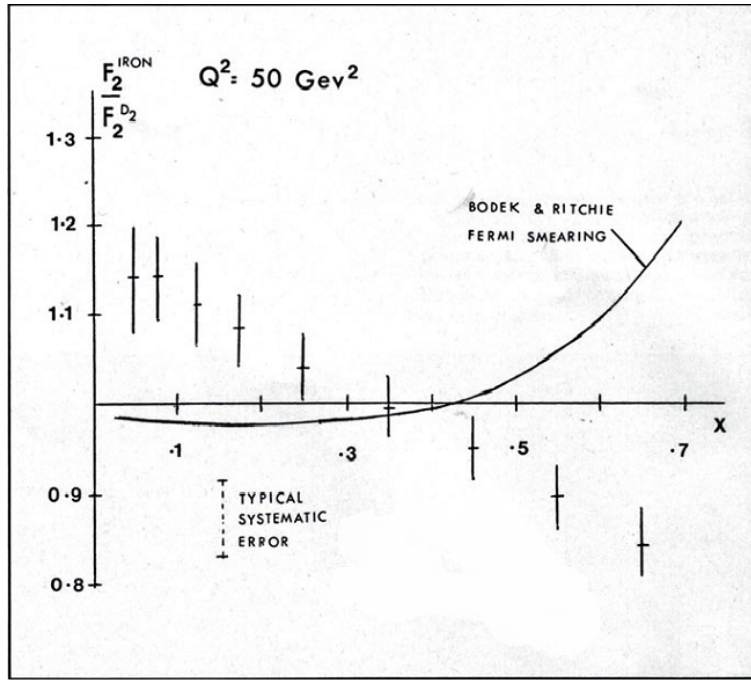
The European Muon Collaboration (EMC) performed a deep inelastic measurement
 with 120-280 GeV muons on iron and deuteron targets [14]. The EMC extracted A/D
 structure function ratios versus the Bjorken scaling variable, x . The relationship
 originally expected by the EMC contained the sum of the structure functions of each
 nucleon in a nucleus. Each nucleus has a certain number of neutrons (N) and a amount
 of protons (Z). The expected structure function for a nucleus could be written as:

$$F_A = NF_2^N + ZF_2^P. \quad (1.10)$$

The EMC compared the extracted structure functions from iron and deuterium.
 Their results are shown in Figure 1.2. The $\frac{A}{D}$ structure function ratio showed
 an unexpected downward slope. This phenomenon was titled the EMC effect.
 This finding demonstrated to the EMC that their understanding of the nucleus

²⁴³ was incorrect. A nucleon's structure function and thereby, the constituent quark distributions may be altered by the nucleus.

Figure 1.2: Graph of the ratio of A/D structure functions vs x for Carbon [10].

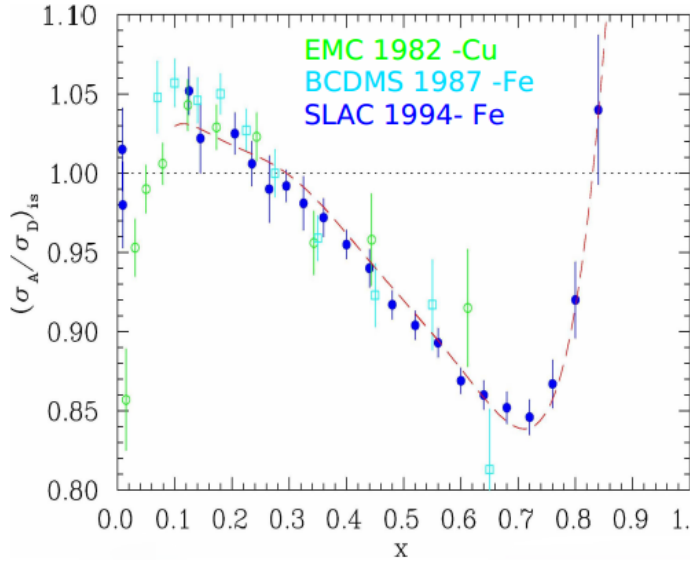


²⁴⁴

²⁴⁵ Ever since the European Muon Collaboration discovered the depletion of quarks at
²⁴⁶ high x for $A > 2$ nuclei, physicists have tried to discover its cause. Scientists at SLAC
²⁴⁷ extracted structure function ratios for many nuclei including; ${}^4\text{He}$, ${}^9\text{Be}$, ${}^{12}\text{C}$, ${}^{27}\text{Al}$,
²⁴⁸ ${}^{40}\text{Ca}$, ${}^{56}\text{Fe}$, ${}^{108}\text{Ag}$, and ${}^{197}\text{Au}$. There were slightly different results for each nucleus.
²⁴⁹ The magnitude of the EMC effect, taken to be the A/D ratio at $x = 0.6$, was found
²⁵⁰ to be different for the various nuclei, and roughly scaled with the size or density of
²⁵¹ the nuclei. The NMC (New Muon collaboration), another group at CERN, gathered
²⁵² precise data in order to construct the inclusive cross section of deuterium and protons.
²⁵³ BCDMS collaboration extracted data for N and Fe structure function ratios. Figure
²⁵⁴ 1.3 shows some of the data from SLAC and BCDMS on the EMC effect for Iron
²⁵⁵ and Cu. Figure 1.4 shows this result from a recent JLab EMC measurement, most
²⁵⁶ precise to date. Many models over the years have been able to reproduce the shape

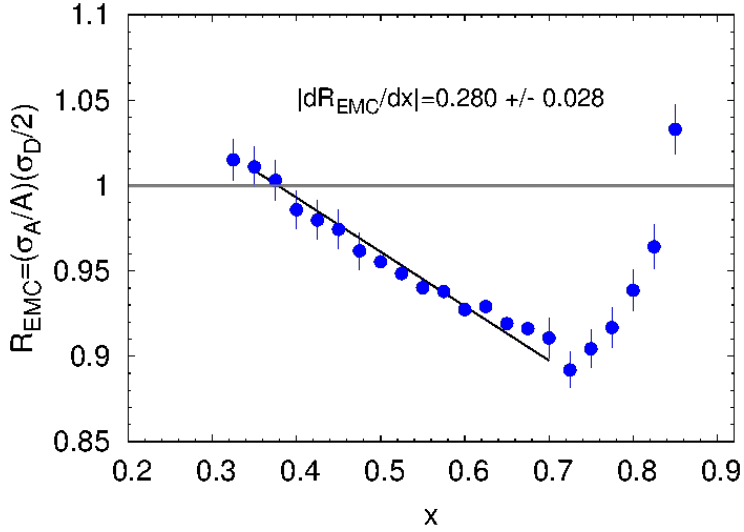
257 of the A/D ratios. These models can contain traditional nuclear physics effects like
 258 momentum distribution or pion-charge contributions. Some models also describe the
 259 EMC effect through quark momentum distribution or modification of the internal
 260 structure [17, 5, 2, 8, 9]. However, no single model has provided a complete picture
 261 of the possible underlying physics. Precise data from Jlab's E03-103 experiment has
 262 revitalized this research. This experiment focused on precision measurements in light
 263 nuclei and added ${}^3\text{He}$ as a target nucleus. Instead of taking the A/D ratio at a
 264 certain x -value to be the magnitude of the EMC effect, this analysis looked at the
 265 slope instead. This eliminated sensitivity to normalization uncertainties.

Figure 1.3: EMC effect from EMC, SLAC, and BCDMS [17]



266 In Figure , ${}^9\text{Be}$ was found not to follow the previously observed scaling with
 267 nuclear density. This result from Jefferson Lab determined that the previous idea
 268 of a dependence on A or nuclear density in the EMC effect to be incorrect [20]. This
 269 result spawned a drive to determine another explanation for the EMC effect and
 270 understand what clue the ${}^9\text{Be}$ outlier was providing. The structure of this nucleus
 271 is made up of two high-density alpha particles and a single neutron [3]. The regions

Figure 1.4: Graph of the ratio of A/D structure functions vs x for Carbon [10].



272 of higher density that are contained in a comparatively large volume may be able to
 273 explain why ${}^9\text{Be}$ does not follow the expected trend. This suggests that the EMC
 274 effect could be a function of local nuclear density [20].

275 1.3 MARATHON

276 Experiment E12-010-102, MARATHON (MeAsurement of the $F2^n/F_2^p, d/u$ RAtios
 277 and A=3 EMC Effect in Deep Inelastic Electron Scattering Off the Tritium and
 278 Helium MirrOr Nuclei), will use deep inelastic scattering off of the mirror nuclei ${}^3\text{H}$
 279 and ${}^3\text{He}$ to measure the EMC effect for both ${}^3\text{H}$ and ${}^3\text{He}$, to determine the ratio of
 280 the neutron to proton inelastic structure functions, and to find the ratio of the down
 281 to up quark distributions in the nucleon.

282 **Chapter 2**

283 **Experimental Setup**

284 **2.1 Thomas Jefferson Lab**

285 Thomas Jefferson Lab (Jlab) in Newport News, Virginia hosted the MARATHON
286 experiment in the Fall of 2017 and Spring of 2018. Jlab uses support from the U.S.
287 Department of Energy(DOE) and the state of Virgina to complete the lab's mission of
288 delivering productive research by exploring the atomic nucleus and its fundamental
289 constituents, including precise tests of their interactions. Along with applying an
290 advanced particle accelerator, particle detectors and other technologies to develop
291 new basic research capabilities and to address the challenges of a modern society.

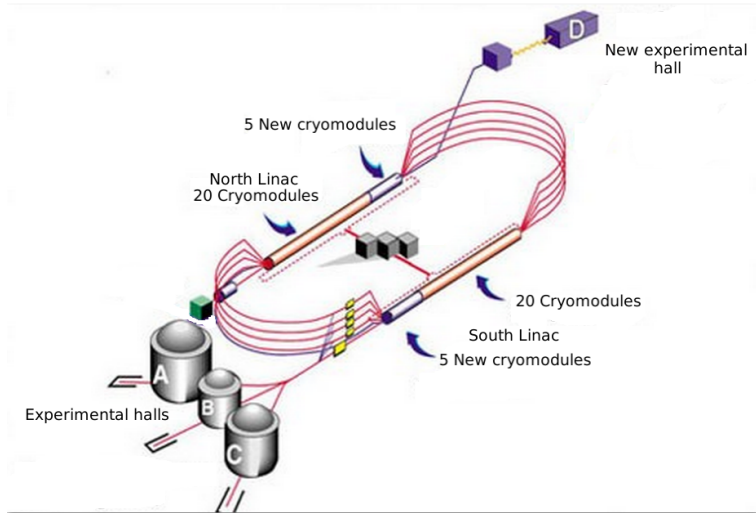
292 **2.1.1 CEBAF**

293 The Continuous Electron Beam Accelerator Facility (CEBAF) was recently
294 upgraded to a 12 GeV accelerator, upgrading it to be able to supply a 11 GeV beam
295 of continuous electrons of up to $200 \mu\text{A}$ of current to three experimental halls (A,B,C)
296 and 12 GeV to the recently constructed hall D. After being accelerated to 45 MeV by
297 a polarized electron gun or a thermionic injector, the electrons are injected into the
298 North linear accelerator (LINAC), shown in figure 2.1. The polarized gun can supply
299 electrons with up to 80% polarization and the polarization direction can be controlled

300 by a wien filter. To ensure the level of polarization, a 5 MeV Mott polarimeter may
301 be used to measure the level of polarization[1].

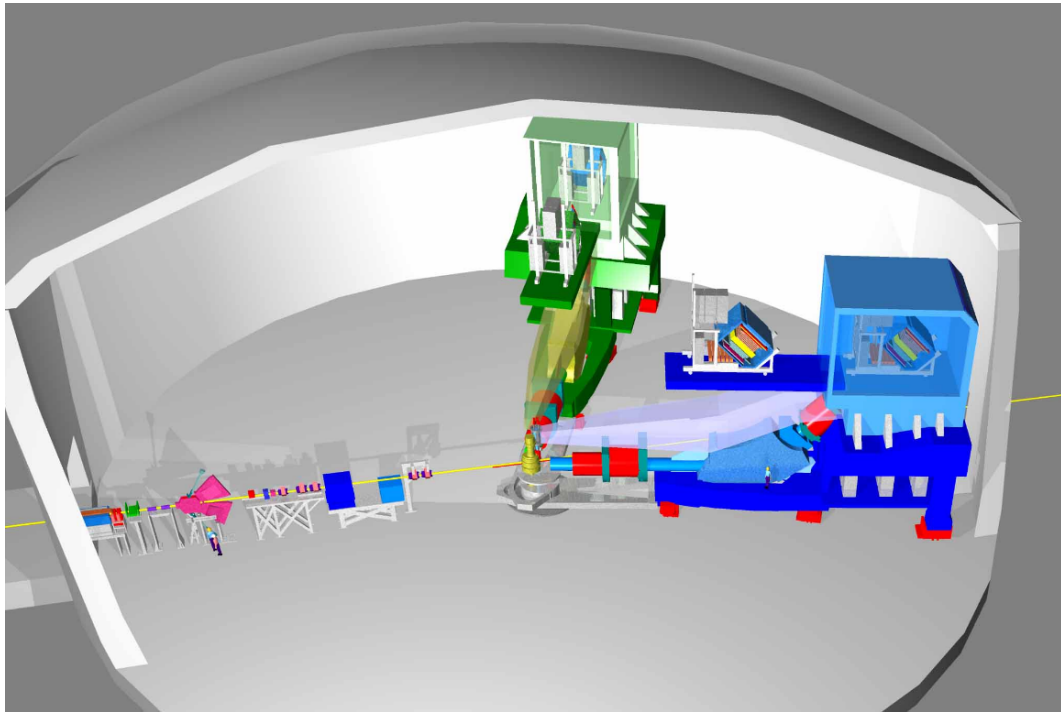
302 The electrons are conveyed through two LINACs and two bending arcs per complete
303 pass of the accelerator. Electrons traveling to Halls A, B, and C complete a maximum
304 of four and a half revolutions around the accelerator. Electrons going to all D travel
305 through the north LINAC for an extra boost. These particles receive approximately
306 2.2 GeV in energy for each cycle through the accelerator. The radio frequency (RF)
307 cavities in each LINAC use an oscillating electromagnetic field to supply a force to
308 accelerate the passing electrons. These Niobium RF cavities are cooled to 2 K in
309 order to create conditions that allow the cavities to be superconducting [1].

Figure 2.1: Schematic Layout of CEBAF.



₃₁₀ **2.1.2 Hall A**

Figure 2.2: A 3D drawing of Hall A.

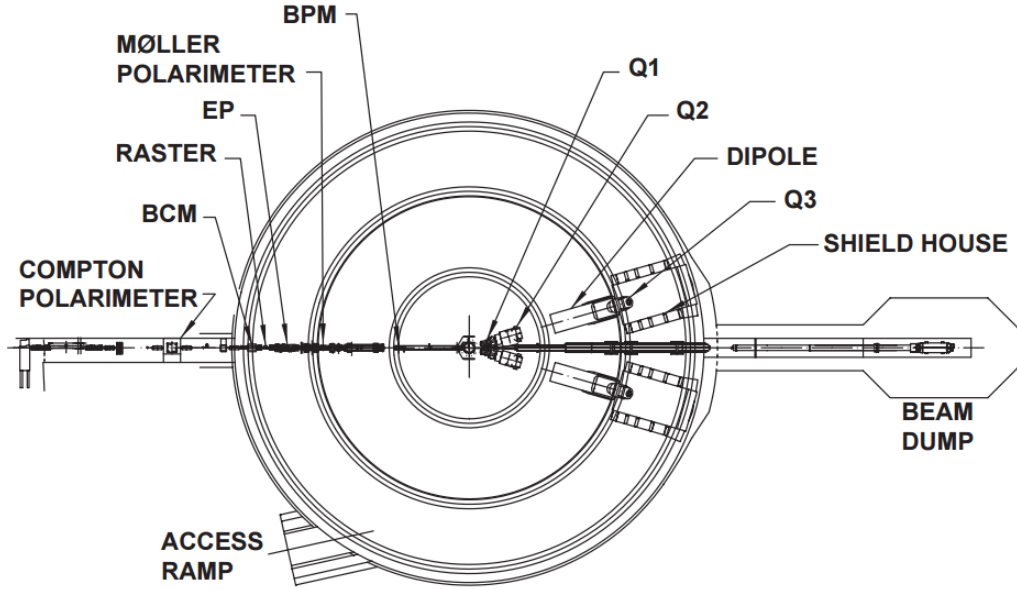


₃₁₁ The experimental Hall A and the scientific equipment used were designed for
₃₁₂ detailed investigations of the internal structure of nuclei. Two high resolution
₃₁₃ spectrometers in Hall A use the inclusive (e,e') and exclusive $(e,e' p)$ reactions to gain
₃₁₄ a greater understanding of the structure of the nucleus. Completing detailed studies
₃₁₅ with high resolution and extreme accuracy requires knowing the beam position, size,
₃₁₆ energy, current, direction, and polarization when the beam strikes the target. The
₃₁₇ instrumentation used in the precise measurement of these quantities in Hall A are
₃₁₈ shown in figure 2.3 [1].

₃₁₉ A pair of Beam Position Monitors(BPM)s are used to measure the relative beam
₃₂₀ position without affecting the beam. The two Hall A BPMs are located at 7.524 m
₃₂₁ and 1.286 m away from the target. Using the standard difference-over-sum technique,
₃₂₂ the relative beam position is determined with an accuracy of 100 μm with a beam

323 current of at least $1 \mu\text{A}$ [1]. The BPMs' positional data is recorded in two ways.
 324 Every second of beam time, the beam position average over 0.3 seconds is logged
 325 into the Experimental Physics and Industrial Control System (EPICS) database.
 326 The BPMs also transmit data event-by-event to the CEBAF online Data Acquisition
 327 system(CODA).

Figure 2.3: A schematic layout of the beam line in Hall. [1]



328 The main beam line components of the BPMs consist of four open-ended antennas.
 329 Figure 2.4 shows a BPM chamber and figure 2.5 shows the layout of the four antennas
 330 as you look down the beam line. In this chamber, the design of three of the four
 331 antennas can be seen. The antennas are titled u_+ , u_- and v_+ , v_- . The antennas
 332 receive an induced signal as electrons pass to determine the beam position in the
 333 u and v directions. The direction of the beam is determined by using the two
 334 BPMs in conjunction with timing information provided. The accuracy of the BPMs
 335 requires an absolute measurement of the electron beam's position to calibrate the
 336 BPMs and a internal input oscillation measurement names twiddle to supply BPM
 337 signal coefficients. [19, 23].

Figure 2.4: BPM design diagram, from JLab instrumentation group. Beam direction is from left to right [23].

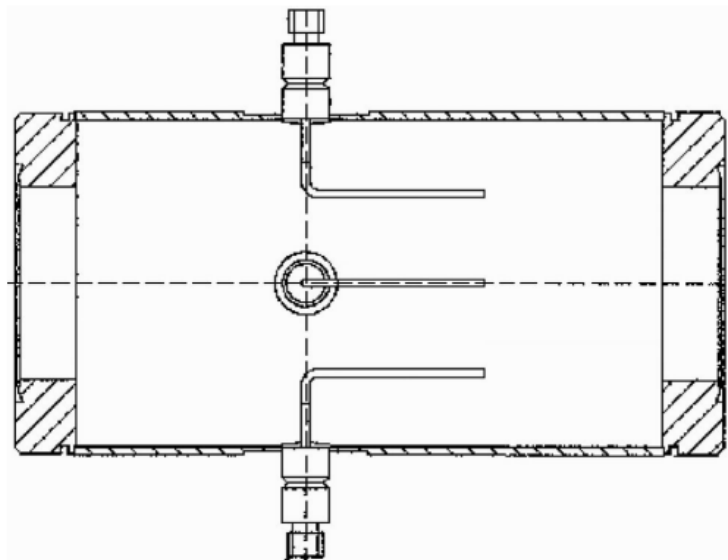
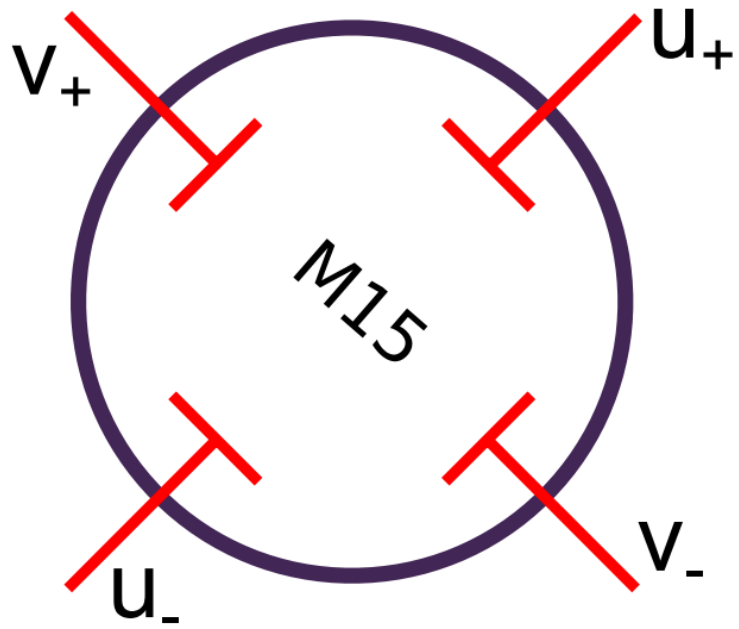


Figure 2.5: BPM design diagram, looking down the beam line[23].



³³⁸ Damage to a target system from intense beam can cause extreme fluctuations in
³³⁹ the target's temperature and density. A raster was used to counteract the damage

340 caused by a focused beam. The raster used two magnetic fields produced by two
341 dipoles to spread the electron beam out. This produces a large rectangle interaction
342 area on the front face of the target container. A triangle wave of 25 kHz was used to
343 control the coils of the dipole magnets. The raster systems are located \approx 17 meters
344 before the target chamber (upstream of the target[23]). The rasters position can be
345 seen in figure 2.2. Safety constraints administrated by the target group at JLAB
346 limited the minimum size of the raster spot for the MARATHON experiment to two
347 millimeters by two millimeters. This limit was installed has a safety concern for the
348 tritium target.

349 The Hall A raster system consists of four dipoles. Two dipoles produce magnetic
350 fields in the horizontal direction of the lab frame and two in the vertical. The upstream
351 raster and downstream rasters include one vertical and one horizontal dipole. The
352 relative change in position of the incoming electrons are controlled by the current
353 supplied to the dipoles. In order to obtain the change in beam position due to the
354 rasters, a calibration between the raster current and measured beam position were
355 obtained.

356 The electron beam energy is located in many of the equations used in an electron
357 scattering experiment. This can cause a noticeable increase in systematic error if the
358 beam energy measurement is not made precisely. At JLAB for the MARATHON
359 experiment, the beam energy was measured in two ways. In Hall A, the beam energy
360 was measured by using the (e,e/p) method. On the beam line, 17 meters upstream
361 from the target an ep scattering chamber is located. The beam was directed into the
362 target containing a rotating 10-30 μ m thick tape of CH_2 . The scattering angle of the
363 electron and the recoil angle of the proton are used to determine the beam energy
364 using equation 2.1. Where M_p is the mass of the proton and θ_p, θ_e are the scattered

³⁶⁵ angle of the proton, electron respectively.

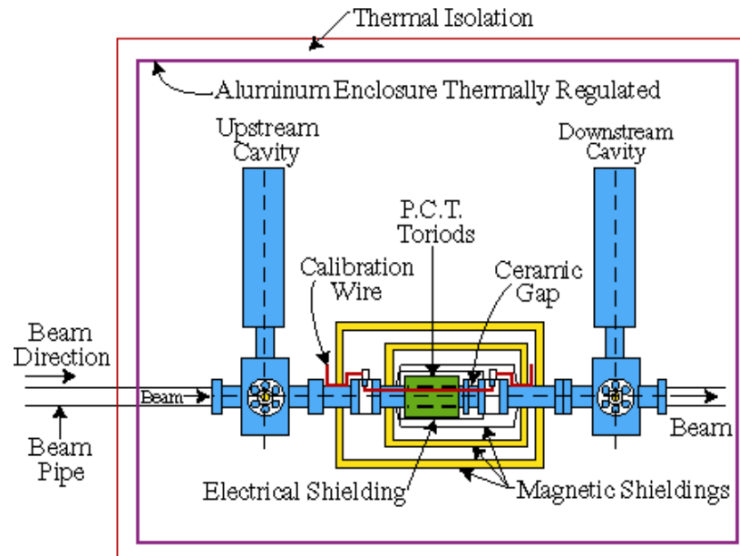
$$E = Mp \frac{\cos\theta_e + \frac{\sin\theta_e}{\tan\theta_p} - 1}{1 - \cos\theta_e} \quad (2.1)$$

³⁶⁶ The beam energy was also measured using the ark measurement method [7]. This
³⁶⁷ method uses changes in beam position and precise measurements of the magnetic
³⁶⁸ fields around the beam line to determine the energy of the electron beam. The angle
³⁶⁹ at which the electrons are bent through is related to the momentum of the electrons,

$$p = k \frac{\int \vec{B} \cdot d\vec{l}}{\theta}. \quad (2.2)$$

³⁷⁰ In equation 2.2, p is the momentum of the electrons, θ is the bend angle, and \vec{B}
³⁷¹ is the magnetic field the electron experiences. Then using the momentum of the
³⁷² electron, the energy of the beam can be extracted. The error on the beam energy
³⁷³ measurement is $\delta E/E \approx 2 * 10^{-4}$ [22, 7]. The MARATHON experiment used both
³⁷⁴ methods to accurately determine the electron beam energy.

Figure 2.6: Hall A Current Monitor components [4].



375 The main process of measuring the scattering yield for a calculation of a cross
376 section looks at finding the ratio of the number of electrons scattered to the number
377 of electrons sent. In order to accurately determine the number of electrons sent to
378 scatter with our target system, Hall A use a highly accurate and non-invasive beam
379 current monitor(BCM). The Hall A BCM has an absolute accuracy of 0.2 percent
380 as long as the current is between 1 and 180 μ A. The BCM used in Hall A consists of
381 three main components: a Parametric Current Transformer (PCT) and two pill box
382 cavities. Figure 2.6 shows the components in the Hall A BCM. The BCM produces
383 an RF signal that is proportional to the beam current. An 10 kHz down converter,
384 RMS-to-DC converter, voltage-to-Frequency converter, and a scaler are used to inject
385 the current signal into the Hall A DAQ. Proportionality constants are determined in
386 the calibration process to correctly integrate the charge for a given amount of beam
387 current[4]. Continue after the initial beam line components, an electron will enter
388 into the target chamber, housing the target system.

389 2.2 Target

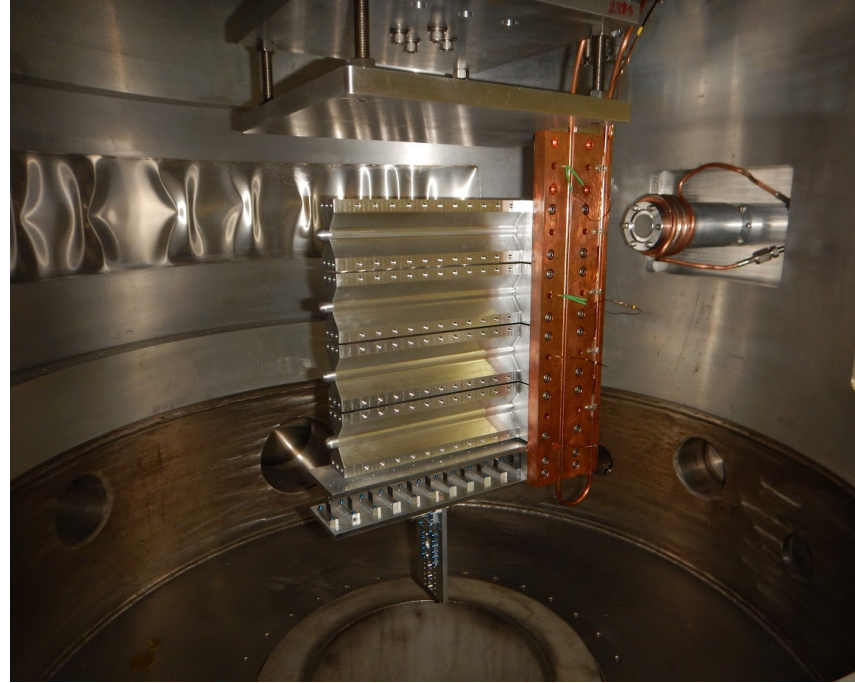
390 The Hall A Tritium Target(HATT) system was used for the Tritium run group of
391 experiments. The HATT target chamber was repurposed from a previously used cryo-
392 target chamber in order to reduce the financial cost of designing a new target chamber.
393 The refurbishing of the cryo-target chamber consisted of adding in new safety features
394 to prevent and mitigate a tritium leak. A 4 inch long collimator with an inner diameter
395 of 0.4 inch was added inside of the target chamber but upstream of the target ladder
396 to prevent the beam from striking the thin side wall of the aluminum cell. In case of
397 a tritium leak in the target chamber, an exhaust system was installed to control the
398 amount of tritium exposed to the Hall.[16] Figure 2.7 shows the HATT system with
399 the target ladder in the home position and the scattering windows removed. A picture
400 of the HATT ladder installed in the HATT system is shown if figure 2.7. The ladder
401 contains both gaseous cells and solid targets. The MARATHON experiment had five

Figure 2.7: Target Images

(a) A image of the HATT. [11]



(b) Image of the Hall A Tritium Target Ladder. [11]



402 gas cells. The top four of the gas cells were filled with tritium, deuterium, hydrogen,
403 and $^3\text{helium}$, from top to bottom respectively. Due to safety restricts the tritium
404 cell was not installed until the HATT system could be closed. The bottom most
405 cell was left empty, to complete end cap subtractions. The lower half of the target
406 ladder contains the solid targets used during the MARATHON experiment. Listed
407 from top to bottom, the solid targets used were a pair of thick aluminum foils, carbon
408 multifoil, single carbon foil, and a carbon foil with a 2mm diameter hole. The thick
409 Al foils were used to aid the target window background subtraction. The multifoil
410 target also know has the optics target was used to calibrate the z-axis reconstruction
411 of the optics matrix. The single carbon foil and carbon hole were used to calibrate
412 the BPMs and rasters and to determine the off set of the central line of the detector.

413 2.3 High Resolution Spectrometers

414 Electrons that successfully scatter from the target may end up in either of the two
415 HRSs(High Resolution Spectrometers). The HRSs were designed to detect charged
416 particles with a high degree of precision. In order to achieve a high level of resolution
417 in momentum and angle, the HRSs were designed with a magnet configuration of
418 QQD_nQ (quadrupole, quadrupole, dipole, and quadrupole). The vertical bending
419 dipole provides the field required to transport the scattered particles through the
420 45° bending angle to the detector hut. A drawing of an HRS can be seen in
421 figure 2.8. The first quadrupole(Q1) focuses the incoming electrons in the vertical
422 plane. The following two quadrupoles (Q2 and Q3 provide transverse focusing. This
423 optical design allows the use of extended gas targets with no substantial loss in solid
424 angle[1]. The spectrometers were designed to perform various functions which include:
425 triggering the data acquisition system (DAQ) when certain requirements are met,
426 gathering the position and direction of individual particles to reconstruct a track,
427 provide precise timing information for time of flight calculations, and identify many
428 different particle types that pass through the detector system. In order for both
429 the Left HRS (LHRS) and Right HRS (RHRS) to complete the required task, they
430 contain a myriad of detectors. The HRSs use drift chambers, scintillators, cerenkov
431 detectors, and shower calorimeters. Both the Left and Right HRSs contain two planes
432 of scintillators to function has the main trigger for the detector package. The vertical
433 drift chambers (VDC) that lay at the front of the detector in conjunction with the
434 Shower that lies in the back of the detector provide information for reconstructing the
435 particle tracks and precise timing. Particles are identified by the cerenkov, shower
436 calorimeters, and pion rejectors that are contained in the left or right HRS. The
437 layout of the individual detectors that make up the left and right detector package
438 are shown in figure 2.9 [1].

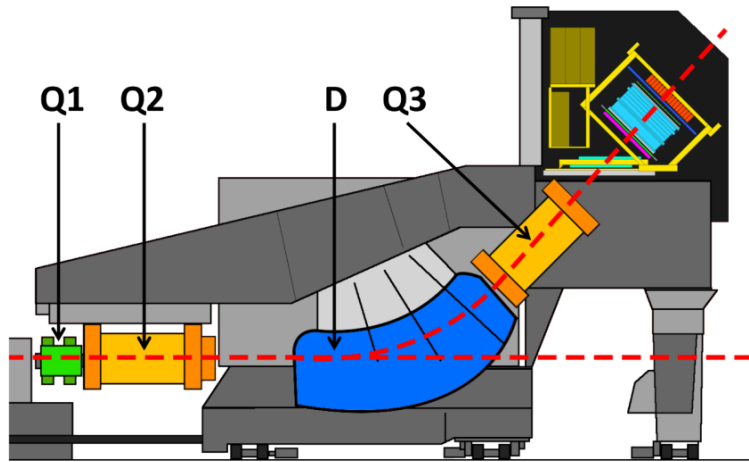


Figure 2.8: A side view of a HRS [1].

⁴³⁹ 2.3.1 Vertical Drift Chambers

⁴⁴⁰ Each of the spectrometers housed in Hall A contains a vertical drift chamber(VDC).
⁴⁴¹ Each VDC contains two planes of crossing sense wires. Shown in figure 2.10, the two
⁴⁴² planes of the VDC lie a distance of 0.335m apart [6]. The lower plane of the VDC
⁴⁴³ is positioned at the approximate focal plane of the HRS and lies in the horizontal
⁴⁴⁴ plane of the Hall A coordinate system. The sense wires located in the VDCs cross
⁴⁴⁵ orthogonally. They are offset by 45° in respect to the dispersive and non-dispersive
⁴⁴⁶ directions.

⁴⁴⁷ [6]

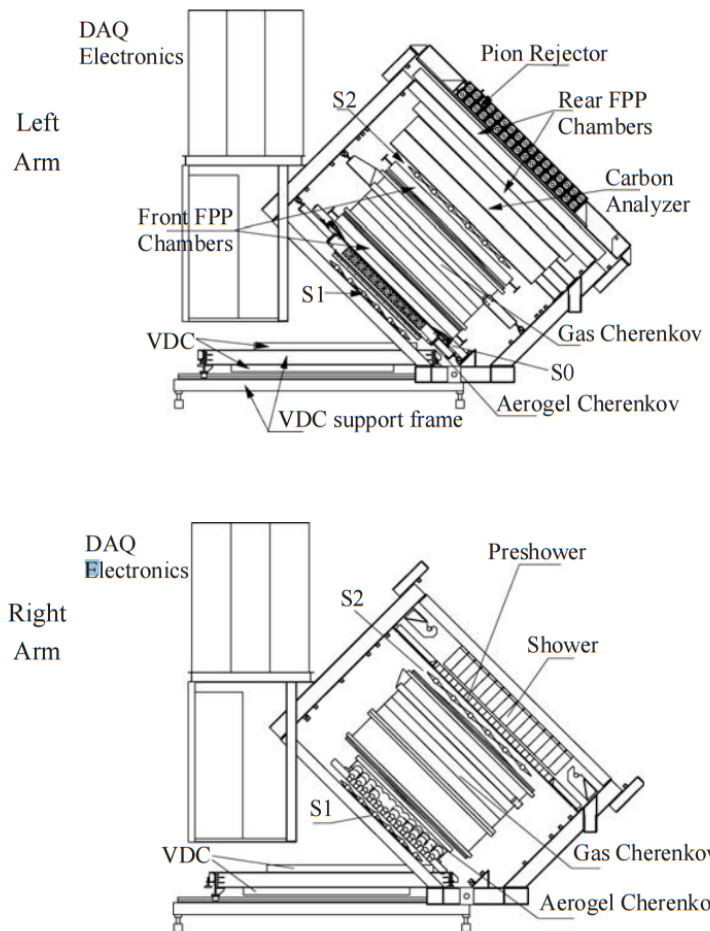


Figure 2.9: A view of both the left (top) and right (bottom) detector stacks inside the left and right HRS [1].

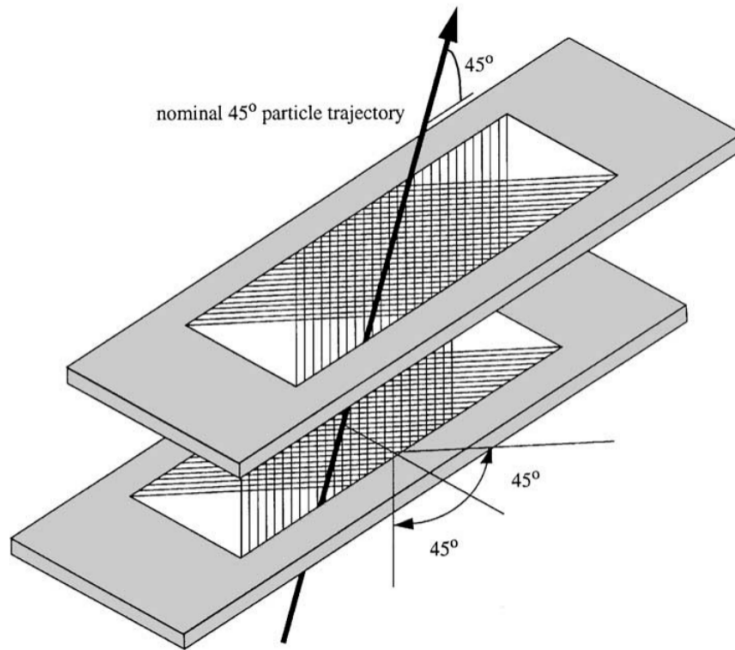


Figure 2.10: A sketch of the two VDC planes in the HRSs with a particle traveling through the detector at 45° .[6].

448 **2.3.2 Scintillators**

449 **2.3.3 Cherenkov**

450 **2.3.4 Shower Calorimeter**

451 **2.3.5 Pion Rejector**

452 **2.3.6 FPP Chambers**

453 **2.4 Trigger Setup**

454 **2.5 DAQ - Data Acquisition System**

455 **2.6 Kinematic Settings**

456 **Chapter 3**

457 **Calibration**

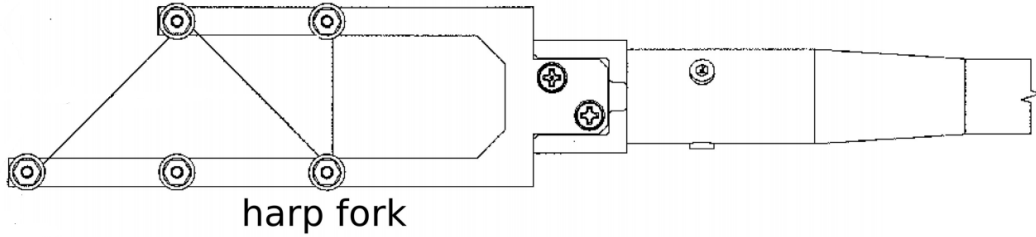
458 The information provided by the detectors originate through small changes in
459 current and voltage sent through the DAQ electronics. These signals are transformed
460 into useful information through calibration constants. The beam line elements and the
461 individual detector components were calibrate to supply highly precise and accurate
462 data.

463 **3.1 Beam Line**

464 The BPM signal coefficients are determined by a twiddle measurement. An RF
465 module attached to the BPM antennas is used to pass a signal out of each of the
466 antennas, one at a time. This will allow the determination of the conversion factor
467 for the BPM signal to relative beam position. Two harps were used to provide
468 the absolute measurement required for calibrating the BPMs. Figure 3.1 contains a
469 drawing of the harps used in Hall A. The harps were moved into the beam line when
470 calibration data is needed, but must be moved out for the production of experimental
471 data because the harp wires are intrusive to the beam operation. The harp forks are
472 aligned perpendicular to the beam line, to allow the harps to be moved in and out of
473 the beam line. Three different wires are used to determine the horizontal and vertical
474 position of the beam. Each wire has one of three orientations: vertical, sloped down

475 or sloped up. The two sloped wires are angled at 45° relative to the wire frame. As
 476 the harp fork is moved into the beam, the wires receive a signal as the beam interacts
 477 with the wires. The two sloped wires are used together to determine the vertical
 478 position of the beam. The vertical wire is used to determine the horizontal position
 479 of the beam [19, 23].

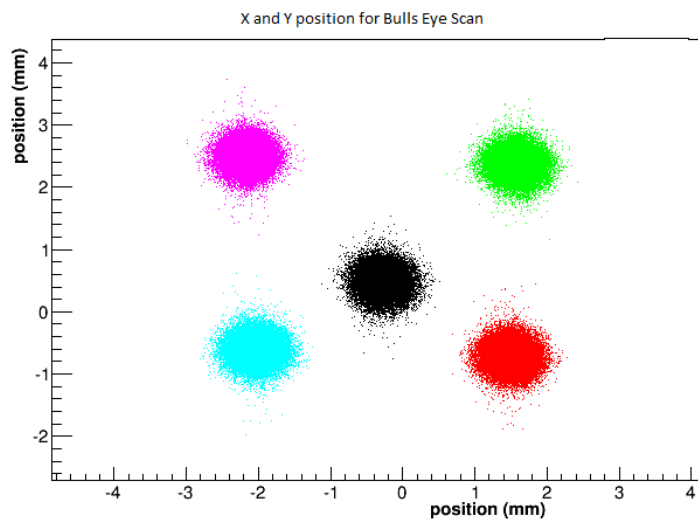
Figure 3.1: A schematic layout of a harp fork [23]



480 The location of the wires on the harp frame and the position of the harp fork
 481 were used to calculate the absolute beam position. The BPM calibration coefficients
 482 were determined by using a bulls eye scan, figure 3.2 shows an example of the five
 483 positions used to calculate the BPM calibration coefficients. The harp scan results
 484 are substituted into equation 3.1 for the X and Y positions. Using all five points and
 485 an R^2 regression technique, the coefficients can be determined with great accuracy.
 486 These highly accurate BPMs were crucial in reducing systematic error in the final
 487 results obtained from this experiment.

$$\begin{pmatrix} X_{position} \\ Y_{position} \end{pmatrix} = \begin{pmatrix} C(0, 0) & C(0, 1) \\ C(0, 0) & C(0, 1) \end{pmatrix} * \begin{pmatrix} X_{BPM} \\ Y_{BPM} \end{pmatrix} + \begin{pmatrix} X_{offset} \\ Y_{offset} \end{pmatrix} \quad (3.1)$$

Figure 3.2: The X and Y position for a Bulls eye scan for BPM calibration.



488 Chapter 4

489 Data Analysis

490 Chapter 5

491 Results

492 **Chapter 6**

493 **Simulation**

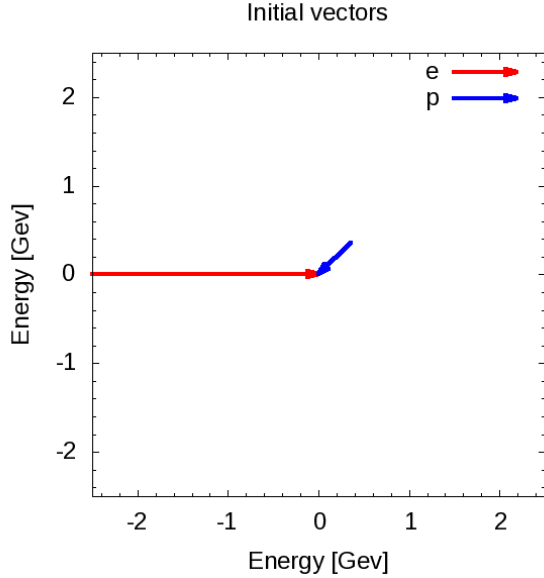
494 Nuclei are systems of nucleons that interact strongly. The characteristic scale for the
495 nucleons momentum is approximately the Fermi momentum, $k_F \approx 200 - 270 \text{ MeV}/c$
496 [9]. However because of the strongly repulsive nature of the nucleon-nucleon
497 interaction at short distances prevents two nucleons from laying in close proximately
498 to each other. This strong interaction demands the presence of high-momentum
499 components in the nuclear ground state wave function. A simulation was designed
500 to phenomenologically study the effect of these high-momentum components on the
501 nuclear EMC effect. This program was designed in two phases. The first phase used
502 simple elastic scattering and a single value for the targets momentum to investigate
503 overall effect of different target momentum on the yield in bins of x_B . The second
504 phase of the simulation was created to lay out the effect of using different momentum
505 distributions on the yield for the EMC effect region of x_B , 0.3 to 0.7.

506 **6.1 Investigation**

507 This simulation phenomenologically investigates the effect of a moving target on the
508 EMC effect by scattering a beam of electrons off of a moving proton. The target
509 protons are comprised of a directional vector of 0° to 360° in respect to the incoming
510 electron beam and a momentum between 0 and 1 GeV/c. Figure 6.1 contains a

511 possible event for the simulation. The electron approaches with 2.5 GeV of energy
512 and collides with a proton moving with a momentum of 0.5 GeV/c with an angle of
45° in respect to the electron trajectory.

Figure 6.1: Example of the electron beam(red) with a energy of 2.5 GeV and the proton(blue) with angle of 45° in respect to the electron and with a momentum of 0.5 GeV/c.



513
514 Using conservation of momentum and conservation of energy in elastic collisions,
515 this simulation calculates the final state of the electron and proton after the scattering
516 event by randomly selecting a scattered direction for the electron. The vector
517 representation of the scattered products are shown in figure 6.3a. In order to
518 make these calculations systematic and to study cross sections models the simulation
519 transform each event into the rest frame of the target before scattering.

520 6.2 Transformation

521 The Simulation completes a set of Lorentz invariant rotations and boost for each
522 event to transform the lab frame of the electron and proton collision into the rest
523 frame of the proton. First the simulation takes the initial proton and electron vectors

524 and rotates them to align the proton vector to the horizontal axis, shown in figure
 525 6.2b. This rotation uses the angle between the proton and the electron defined as λ .
 526 This allows for a straight forward calculations for the Lorentz factors β and γ and
 527 to boost into the rest frame of the target proton, figure 6.2c. Once in the boosted
 528 frame, the angle between the electron and the horizontal axis is defined as δ . Right
 529 before the simulation starts to calculate the scattered products, it completes one more
 530 rotation to align the electron vector with the horizontal axis, figure 6.2d, to make the
 531 scattering calculation systematic and unconditional.

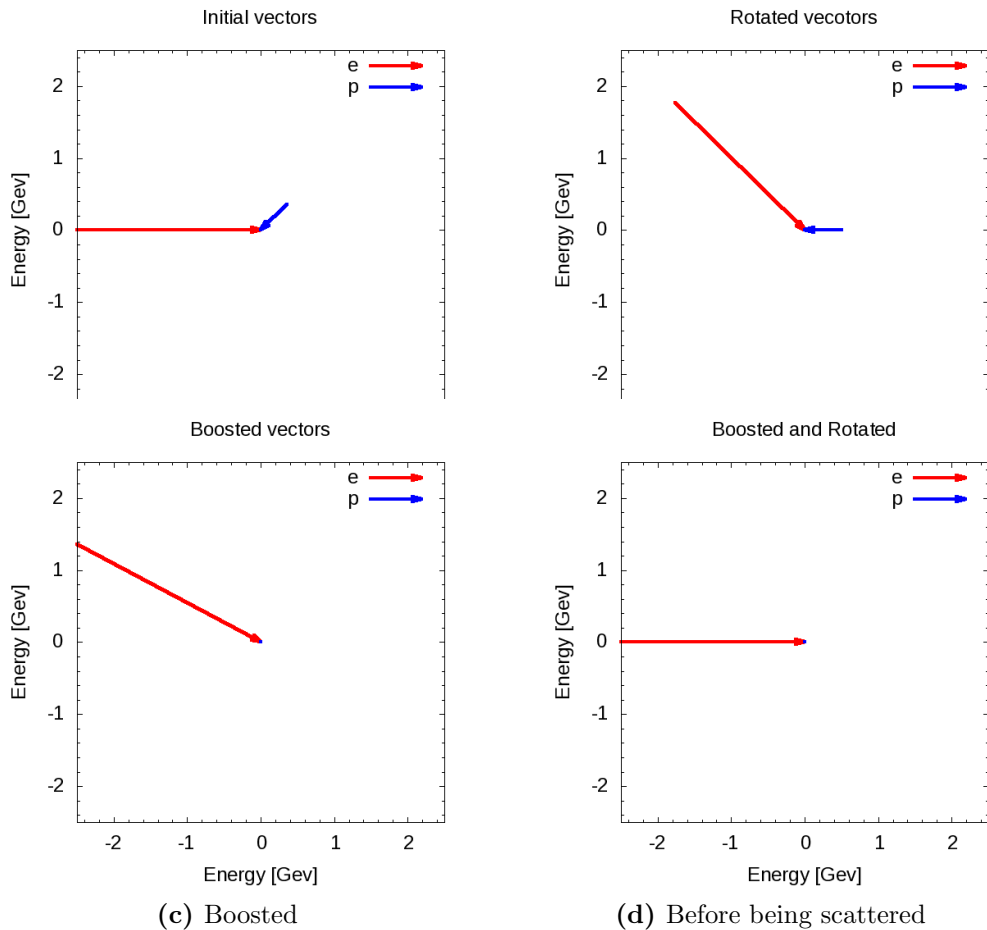


Figure 6.2: Vector representations of the momentum for the incoming electron(red) and target proton(blue) with units of GeV for each phase of their transformations before scattering.

532 In order to gain a more complete understanding of the scattering products, the
533 program completes a set of transformations to move from the rest frame of the target
534 proton to the beginning lab frame. After the simulation calculates the scattered
535 products it begins to transform back by beginning with a rotation by the angle δ ,
536 figure 6.3b. Followed by the inverse of the previously used Lorentz boost. The
537 last transformation, a rotation by λ , transforms the frame back into the lab frame.
538 A proton vector and electron vector in the lab frame are the final products of the
539 simulation. An image of the electron and proton vectors for each transformation can
540 be found in figure 6.3. These vectors allow for calculation of kinematic variables such
541 as Bjorken x and the four-momentum transfer (Q^2). This simulation will complete
542 these steps for many electron and proton combinations.

543 6.3 Results

544 This electron scattering simulation produced results for two stages. The firsts stage
545 used a fix proton momentum for each run to compare the yield in bins of x_B . Figure
546 6.4 shows the results for three different runs, each having a unique fixed proton
547 momentum. The red histogram represents a run with a proton momentum of 0 Gev/c.
548 The result is an elastic peak at x_B of one. The blue histogram contains the results
549 having a fixed proton momentum of 0.25 GeV/c. Increasing the initial momentum
550 of the proton spreads the events into two peaks. The scattering interactions that
551 form the peak above 1 x_B are produced by events were the proton's initial directional
552 vector are orientated towards the electron. The events that produce an x_B below
553 1 have a proton direction pointing away from the electron initially. Doubling the
554 proton's initial momentum from 0.25 GeV to 0.50 GeV causes these peaks two spread
555 out furtherer in x_B .

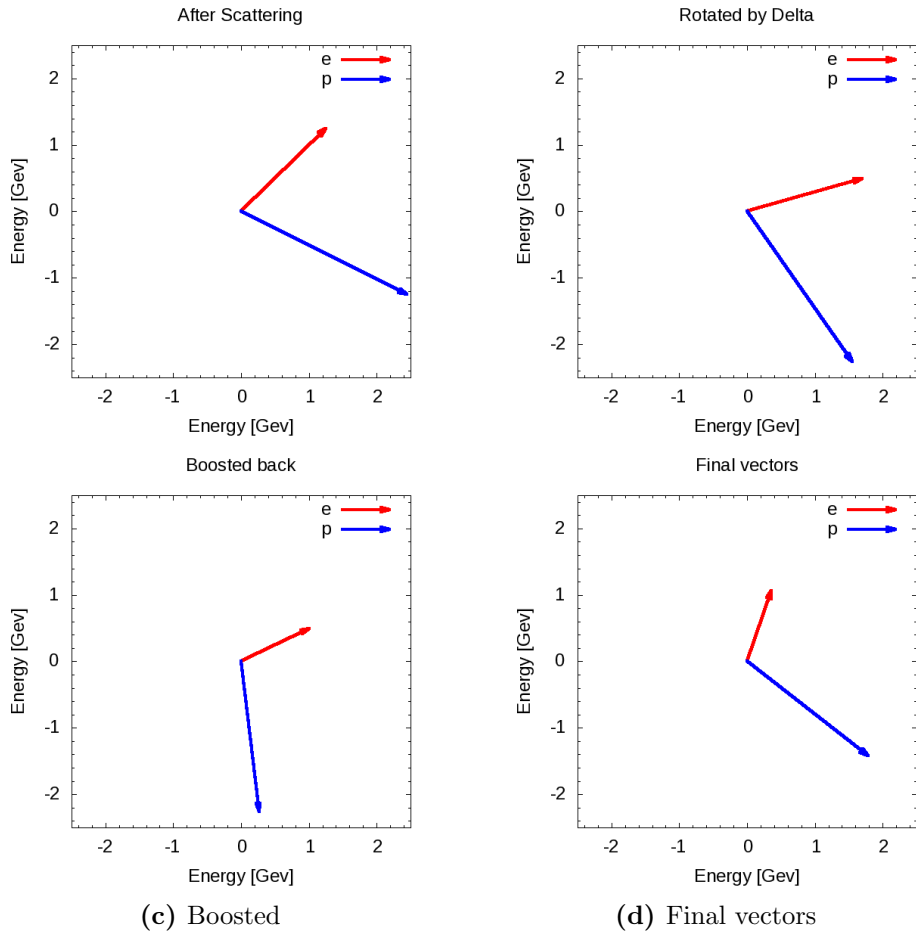
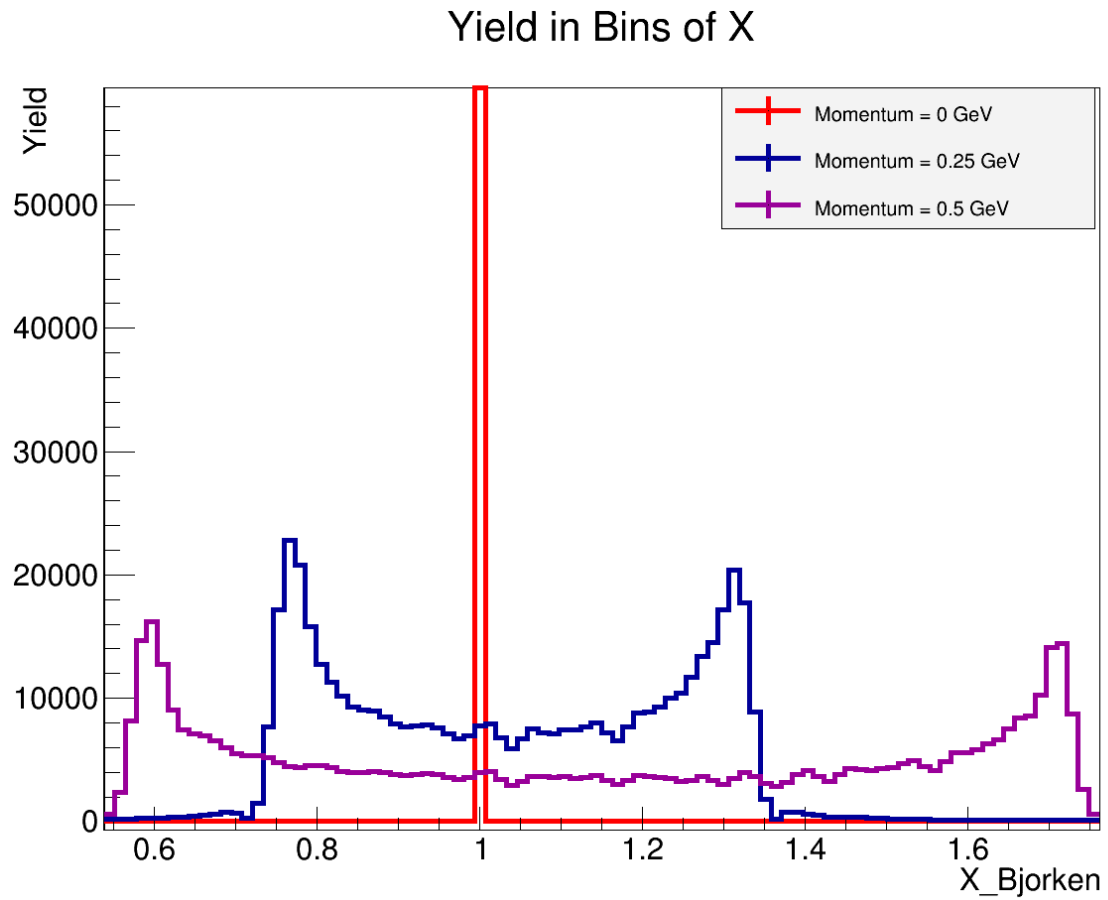


Figure 6.3: Vector representations of the momentum for the incoming electron(red) and target proton(blue) with units of GeV for each phase of their transformations after scattering).

Figure 6.4: Simulation results for fixed momentum protons. Three runs with unique proton momentum.



556 Chapter 7

557 Conclusion

Bibliography

559 **Bibliography**

- 560 [1] J. Alcorn et al. Basic Instrumentation for Hall A at Jefferson Lab. *Nucl. Instrum.*
561 *Meth.*, A522:294–346, 2004. [vi](#), [11](#), [12](#), [13](#), [19](#), [20](#), [21](#)
- 562 [2] John Arrington, Aji Daniel, Donal Day, Nadia Fomin, Dave Gaskell, and Patricia
563 Solvignon. A detailed study of the nuclear dependence of the EMC effect and
564 short-range correlations. *Phys. Rev.*, C86:065204, 2012. [8](#)
- 565 [3] A. Daniel, J. Arrington, and D. Gaskell. Measurements of the EMC effect in
566 few-body nuclei at large x. *AIP Conf. Proc.*, 1369:98–105, 2011. [8](#)
- 567 [4] J. Denard and J. Sahar. High accuracy beam current monitor system for cebaf’s
568 hall a. Chicago, 2001. Particle Accelerator Conference. [vi](#), [16](#), [17](#)
- 569 [5] J. Edelmann, G. Piller, Norbert Kaiser, and W. Weise. Resonances and higher
570 twist in polarized lepton nucleon scattering. *Nucl. Phys.*, A665:125–136, 2000. [8](#)
- 571 [6] K.G. Fissum et al. Vertical drift chambers for the hall a high-resolution
572 spectrometers at jefferson lab. *Nuclear Instruments and Methods in Physics*
573 *Research Section A: Accelerators, Spectrometers, Detectors and Associated*
574 *Equipment*, 474(2):108 – 131, 2001. [vi](#), [20](#), [22](#)
- 575 [7] David J. Flay. *Measurements of the Neutron Longitudinal Spin Asymmetry A1n*
576 *and Flavor Decomposition in the Valence Quark Region*. PhD thesis, Temple
577 University, Philadelphia, PA, Aug 2014. [vi](#), [2](#), [3](#), [16](#)

- 578 [8] D.F. Geesaman, K Saito, and A Thomas. The nuclear emc effect. *Annual Review*
579 of Nuclear and Particle Science, 45(1):337–390, 1995. [8](#)
- 580 [9] J. Gomez et al. Measurement of the A-dependence of deep inelastic electron
581 scattering. *Phys. Rev.*, D49:4348–4372, 1994. [8, 28](#)
- 582 [10] D. Higinbotham. The emc effect still puzzles after 30 years - cern courier.
583 <http://cerncourier.com/cws/article/cern/53091>, April 2013. (Visited on
584 01/04/2016). [vi, 2, 7, 9](#)
- 585 [11] Doug Higinbotham. Target images, December 2017. [18](#)
- 586 [12] R Hofstadter. Nuclear and nucleon scattering of high-energy electrons. *Annual*
587 *Review of Nuclear Science*, 7(1):231–316, 1957. [4](#)
- 588 [13] Henry W. Kendall. Deep inelastic scattering: Experiments on the proton and
589 the observation of scaling. *Rev. Mod. Phys.*, 63:597–614, Jul 1991. [6](#)
- 590 [14] Simona Malace, David Gaskell, Douglas W. Higinbotham, and Ian Cloet. The
591 Challenge of the EMC Effect: existing data and future directions. *Int. J. Mod.*
592 *Phys.*, E23:1430013, 2014. [6](#)
- 593 [15] R. W. McAllister and R. Hofstadter. Elastic scattering of 188-mev electrons from
594 the proton and the alpha particle. *Phys. Rev.*, 102:851–856, May 1956. [2](#)
- 595 [16] David Meekings. Hall a tritium target. Thomas Jefferson Lab, Virginia,
596 engineering Report, 2017. [17](#)
- 597 [17] P R Norton. The emc effect. *Reports on Progress in Physics*, 66(8):1253, 2003.
598 [vi, 8](#)
- 599 [18] Bogdan Povh, Klaus Rith, Christoph Scholz, and Frank Zetsche. *Particles and*
600 *Nuclei: An Introduction to the Physical Concepts*. Springer, 2009. [1, 2, 4, 5](#)

- 601 [19] Tom Powers, Lawrence Doolittle, Rok Ursic, and Jeffrey Wagner. Design,
602 commissioning and operational results of wide dynamic range bpm switched
603 electrode electronics. *AIP Conference Proceedings*, 390(1):257–265, 1997. [13](#),
604 [24](#)
- 605 [20] J. Seely et al. New measurements of the european muon collaboration effect in
606 very light nuclei. *Phys. Rev. Lett.*, 103:202301, Nov 2009. [2](#), [8](#), [9](#)
- 607 [21] Richard E. Taylor. Deep inelastic scattering: The early years. *Rev. Mod. Phys.*,
608 63:573–595, Jul 1991. [6](#)
- 609 [22] Hall A Tech. Ep method. [http://hallaweb.jlab.org/equipment/beam/
610 energy/ep_web.html](http://hallaweb.jlab.org/equipment/beam/energy/ep_web.html). (Accessed on 06/28/2016). [16](#)
- 611 [23] Pengjia Zhu et al. Beam Position Reconstruction for the g2p Experiment in Hall
612 A at Jefferson Lab. *Nucl. Instrum. Meth.*, A808:1–10, 2016. [vi](#), [13](#), [14](#), [15](#), [24](#)

Appendix

613